

Article

Effect of Bi Substitution on Structural and AC Magnetic Susceptibility Properties of $\text{Nd}_{1-x}\text{Bi}_x\text{MnO}_3$

Nurul Atiqah Azhar ¹, Intan Solehah Ismail ¹, Nur Baizura Mohamed ² , Azhan Hashim ² and Zakiah Mohamed ^{1,*}

¹ Faculty of Applied Sciences, Universiti Teknologi MARA, UiTM, Shah Alam 40450, Malaysia; nurulatiqahazhar97@gmail.com (N.A.A.); intansolehah96@gmail.com (I.S.I.)

² Faculty of Applied Sciences, Universiti Teknologi MARA, UiTM, Pahang 26400, Malaysia; nurbaizura620@uitm.edu.my (N.B.M.); dazhan@uitm.edu.my (A.H.)

* Correspondence: zakiah626@uitm.edu.my; Tel.: +60-183-708-386

Received: 1 June 2020; Accepted: 16 June 2020; Published: 17 June 2020



Abstract: This study synthesizes the neodymium-based manganites with Bi doping, $\text{Nd}_{1-x}\text{Bi}_x\text{MnO}_3$ ($x = 0, 0.25$ and 0.50) using the solid-state reaction route. The crystal structural, morphological and magnetic properties were determined using X-ray diffraction (XRD), fourier transform infrared spectroscopy (FTIR), field emission scanning electron microscopy (FESEM) and AC magnetic susceptibility. The Rietveld refinement confirmed that the compounds were in the single-phase orthorhombic structure of the NdMnO_3 with Pbnm space group and lattice parameter b increased with doping from 5.5571 ($x = 0$) to 5.6787 ($x = 0.5$). FTIR spectra showed that absorption bands were located within the range of $550\text{--}600\text{ cm}^{-1}$, which corresponded to the Mn–O stretching vibration. FESEM exhibited homogenous compound. The AC magnetic susceptibility measurement studies showed a strong antiferromagnetic (AFM) to paramagnetic (PM) transition existed at 76 K , 77 K and 67 K for samples ($x = 0, 0.25$ and 0.50), respectively.

Keywords: X-ray diffraction; perovskites manganites; AC magnetic susceptibility

1. Introduction

Existing studies on the family of manganites perovskites, RMnO_3 as a parent of mixed valence perovskites, where R is made up of rare earth elements, such as La, Pr and Nd, were found a few decades ago due to their exotic behavior in electrical and magnetic properties [1,2]. Manganites perovskites were the favorite amongst researchers compared with other families of oxides because of their various possible substitutions that may change their crystal structure and properties [3]. Since the rediscovery of colossal magnetoresistance (CMR), many researchers have been focusing on the doped compound manganites due to their fascinating basis in physics and significance in technological importance, such as magnetic sensors [4]. Few theories have surfaced to explain the CMR mechanisms, such as double exchange (DE), superexchange (SE), Jahn-Teller (JT) effect, polaronic effects and so on.

Primarily, undoped NdMnO_3 is an antiferromagnetic (AFM) insulator with Néel temperature 67.2 K due to the interplay between the ferromagnetic (FM) DE and AFM SE interactions present in the compound [5]. Chatterji et al. confirmed that NdMnO_3 has an A-type AFM structure of the Mn magnetic sublattice below Néel temperature, $T_N \approx 81.7\text{ K}$ [6]. When doped with divalent cations on the Nd sites, for example in $\text{Nd}_{1-x}\text{Ca}_x\text{MnO}_3$, FM semiconducting behavior was observed with $x \leq 0.25$. However, when $x > 0.80$, the compound exhibited AFM semiconducting at low temperatures [7]. For $\text{Nd}_{0.5}\text{Ca}_{0.5}\text{MnO}_3$, the compound undergoes a charge ordering (CO) transition at $T_{CO} = 250\text{ K}$ and the AFM ordering transition at $T_N = 160\text{ K}$, which is consistent with the study done by Wu et al. [7,8]. In this case, both authors suggested that the presence of CO was due to the JT distortion, resulting in

the distortion of MnO_6 octahedral and localization of charge carrier, by decreasing its mobility, which seemed to weaken the DE interaction [7–9]. Meanwhile, when NdMnO_3 was doped with monovalent cations such as Na^+ and K^+ , it showed an FM insulator behavior and CO transition was observed for $\text{Nd}_{1-x}\text{Na}_x\text{MnO}_3$ at -250 K when $x > 0.1$ [5,10]. However, a lack of knowledge still exists on Nd series doped with trivalent cations such as $\text{Nd}_{1-x}\text{Bi}_x\text{MnO}_3$.

Previous studies reported that although Bi^{3+} (1.24 \AA) and La^{3+} (1.22 \AA) have almost similar ionic radii, both systems exhibit different structures and properties [11]. LaMnO_3 exhibited an AFM insulator [12], while BiMnO_3 exhibited an FM insulator with T_C of 105 K – 110 K [11,13,14]. Recent studies on bismuth-doped manganites, such as $\text{La}_{0.7-x}\text{Bi}_x\text{Ag}_{0.3}\text{MnO}_3$ [12], $\text{La}_{1-x}\text{Bi}_x\text{MnO}_3$ [13] and $\text{La}_{0.67-x}\text{Bi}_x\text{Sr}_{0.33}\text{MnO}_3$ [15], showed a decreased metal–insulator transition temperature, T_{MI} , with an increase of Bi content. The author suggested that the behavior of the latter was related to possible hybridization of Bi $6s^2$ lone pairs and e_g electron of Mn^{3+} , which could have affected the localization of carriers and weakened the DE interaction. Moreover, Bi substitution may also reduce the Mn–O–Mn angle, which can block the movement on e_g electron from Mn^{3+} to Mn^{4+} , which decreases the mobility of conduction electron and weaken the DE process [2,12].

Several works were reported on Bi substitution, especially in La-based system, but a lack of study on Bi substitution in Nd-based system still exists, especially for optical and magnetic properties. In this study, we focus on reporting the structural, optical and magnetic properties of $\text{Nd}_{1-x}\text{Bi}_x\text{MnO}_3$ to investigate the unique role of Bi in the system.

2. Materials and Methods

Polycrystalline samples for $\text{Nd}_{1-x}\text{Bi}_x\text{MnO}_3$ ($x = 0, 0.25$ and 0.50) were synthesized by using conventional solid state reaction method. High purity ($\geq 99.9\%$) neodymium oxide (Nd_2O_3), bismuth oxide (Bi_2O_3) and manganese oxide (Mn_2O_3) powders were weighed in stoichiometric ratio using electronic balance and mixed together. Agate mortar and pestle were used to grind the powders for about 2 h before calcination in air at $700 \text{ }^\circ\text{C}$ for 24 h, repeating twice in order to eliminate volatile foreign particles. Finally, the obtained powders were then pressed into pellet under a pressure of 5 tons and were sintered at $1100 \text{ }^\circ\text{C}$ for 24 h.

The structure and phase purity of the samples were observed by using the X-ray diffraction technique (X'pert PRO MPD) at room temperature with $\text{Cu-K}\alpha$ ($\lambda = 1.5418 \text{ \AA}$) radiation by using a PANanalytical diffractometer. The XRD data were analyzed using the Rietveld refinement method using several software programs, such as General Structure Analysis System (GSAS) and Graphical User Interfaces (EXP-GUI) for the refinement and CMPR to convert data from ASC file to DAT file. Fourier transform infrared spectroscopy (FTIR) results were recorded using FTIR–Raman Drift Nicolet 6700 in the range of 450 – 2000 cm^{-1} to directly probe with the functional group present in perovskite samples. Samples were thoroughly mixed in KBr before the characterization. LEO model 982 Gemini Field Emission Scanning Electron Microscopy (FESEM) with energy-dispersive spectroscopy (EDX) were used to determine the surface morphology and homogeneity of the perovskite samples. AC susceptibility (χ') measurements were carried out using a Stanford research model SR-7265 lock-in amplifier and were performed in the temperature range from 30 K to 300 K .

3. Results

3.1. Structural Analysis

This study obtained all the samples of NdMnO_3 doped with Bi as black and well-crystallized powders. Figure 1 shows the XRD patterns for manganites $\text{Nd}_{1-x}\text{Bi}_x\text{MnO}_3$ ($x = 0, 0.25$ and 0.50) that were conducted at room temperature to validate the structure and sample purities and were then analyzed by using the Rietveld refinement technique (Figure 2). All samples were indexed in an orthorhombic structure ($a \neq b \neq c$ and $\alpha = \beta = \gamma = 90^\circ$) with Pbnm space group. The refined patterns were quite acceptable as the obtained value of agreement factor, χ^2 , showed a value of ~ 1 ,

which indicated a good fit. Rietveld refinement showed the samples $x = 0$ and $x = 0.25$ crystallized in a single phase and were chemically pure. However, a small amount of Bi_2O_3 phase was detected in $\text{Nd}_{0.5}\text{Bi}_{0.5}\text{MnO}_3$ sample. The appearance of a secondary phase and redistribution of peak intensities in the $\text{Nd}_{0.5}\text{Bi}_{0.5}\text{MnO}_3$ sample was an indication of incomplete crystallization of the sample at the sintering temperature. The assumed structure for NdMnO_3 was consistent with most previous studies [6,10,16,17] that reported the same structure with Pbna or Pbnm space group (different setting), ICSD No. 153214, 247143. The sharpening of the peaks was due to the better crystallinity of the nanoparticles and only minimal impurities were detected in the XRD pattern of the $x = 0.50$ sample. In addition, the main diffraction peaks corresponded to (121) hkl plane and matched with the previous study [18]. The crystallite size (D) of the samples estimated by the Debye–Scherer equations, $D = K\lambda/(\beta(\theta) \cos \theta)$, where D is the crystallite size (nm), K is constant with 0.94, λ is wavelength of XRD that is 0.1541 nm for $\text{CuK}\alpha$ radiation \AA and β is full-width at half-maximum (FWHM) and θ is the angle of peak of XRD. The average crystallite size was found to be in the range 74–128 nm.

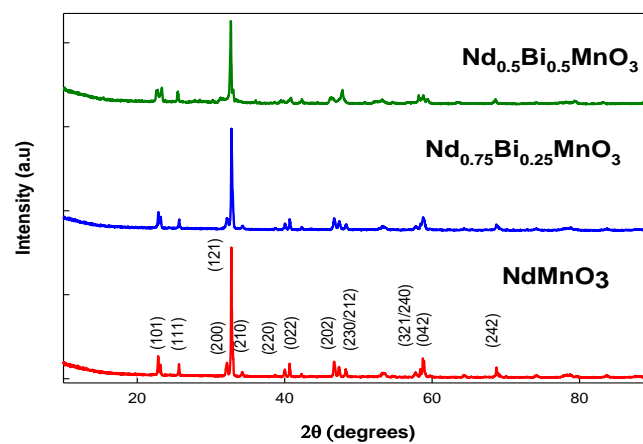


Figure 1. X-ray diffraction of $\text{Nd}_{1-x}\text{Bi}_x\text{MnO}_3$ ($x = 0, 0.25$ and 0.50) samples.

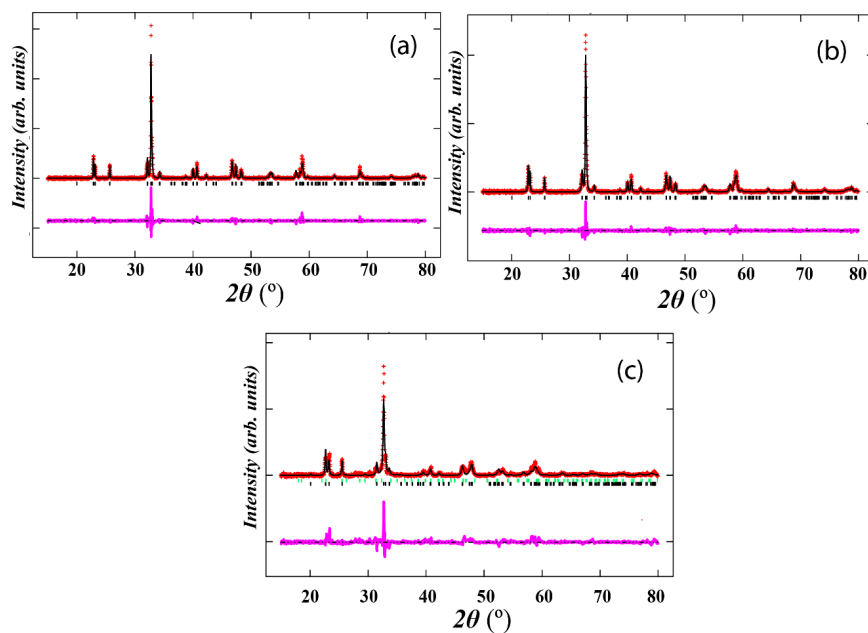


Figure 2. Rietveld refinement for (a) NdMnO_3 , (b) $\text{Nd}_{0.75}\text{Bi}_{0.25}\text{MnO}_3$ and (c) $\text{Nd}_{0.5}\text{Bi}_{0.5}\text{MnO}_3$. Black solid lines are observed data, the solid red line is the calculated patterns and the pink line is the difference. Tick marks indicate the allowed Bragg reflections. Bi_2O_3 impurity phase was detected for $\text{Nd}_{0.5}\text{Bi}_{0.5}\text{MnO}_3$ and indicated by green tick marks.

Table 1 presents the corresponding data of lattice parameters obtained from Rietveld refinement technique. For the undoped sample, the lattice parameters obtained, $a = 5.424 \text{ \AA}$, $b = 5.5570 \text{ \AA}$ and $c = 7.6648 \text{ \AA}$, were found to be quite consistent with the value reported by the previous study [10]. The structural parameter b of the samples increased as the Bi doping increased up to $x = 0.50$. However, for both lattice parameters, a and c showed no systematic trend due to Bi substitution. The unit cell volume of the samples also increased with the increase of the Bi^{3+} substitution. The increases in unit cell volume were suggested due to the Bi substitution at Nd site, where the Bi^{3+} had a slightly larger ionic radius compared with Nd^{3+} and could replace it, which led to the expansion of cell volume [12,13]. Both authors stated that the radius of Bi^{3+} may depend on the character of $6s^2$ lone pairs; it can be seen that when Bi $6s^2$ lone pair is dominant, the ionic radius of Bi^{3+} is 1.24 \AA , while when not, the ionic radius of Bi^{3+} is approximately 1.16 \AA [12]. Hence, the increase in structural parameter, b , and cell volume, V , with Bi substitution suggests that the Bi $6s^2$ lone pair is dominant in the $\text{Nd}_{1-x}\text{Bi}_x\text{MnO}_3$ system. From Table 2, the Mn–O bond length decreased and the average ionic radius, r_A , increased as Bi concentration level increased. However, Mn–O–Mn bond angle showed no trend with the increased Bi-doped. The tolerance factor (τ) was calculated using formula $\tau = (\langle r_A \rangle + \langle r_O \rangle) / \sqrt{2} ((\langle r_B \rangle + \langle r_O \rangle))$, where $\langle r_A \rangle$, $\langle r_B \rangle$ and $\langle r_O \rangle$ represent the average ionic radii of A, B and O sites, respectively [9]. The values of τ showed an increase from 0.515 ($x = 0$) to 0.529 ($x = 0.50$), as seen in Table 2. The increase in τ indicates that a slight reduction of MnO_6 distortion exists, thus the lattice reduced the mismatch between A–O and B–O layer as the Bi concentration increased [18,19].

Table 1. Lattice parameters a , b and c , and cell volume, V , of $\text{Nd}_{1-x}\text{Bi}_x\text{MnO}_3$ samples.

Doping Content (x)	0.0	0.25	0.50
Space group	Pbnm	Pbnm	Pbnm
Symmetry	Orthorhombic	Orthorhombic	Orthorhombic
a (\AA)	5.4240	5.4292	5.4321
b (\AA)	5.5570	5.6534	5.7712
c (\AA)	7.6648	7.6323	7.8536
$\alpha = \beta = \gamma$	90	90	90
Volume (\AA^3)	231.03	234.27	236.25

Table 2. Bond length and bond angle between Mn–O–Mn and goodness of fit for $\text{Nd}_{1-x}\text{Bi}_x\text{MnO}_3$ samples.

Doping Content (x)	0	0.25	0.50
Mn–O ₁ (\AA)	1.9903 (5)	2.0407 (7)	1.9874 (4)
Mn–O ₂ (\AA)	2.0256 (5)	1.9685 (6)	1.9289 (3)
$\langle \text{Mn–O} \rangle$ (\AA)	2.0080 (5)	2.0046 (6)	1.9581 (2)
Mn–O ₁ –Mn ($^\circ$)	148.62(1)	138.45 (3)	148.58 (9)
Mn–O ₂ –Mn ($^\circ$)	154.61(1)	149.36 (12)	154.08 (4)
$\langle \text{Mn–O–Mn} \rangle$ ($^\circ$)	151.62 (1)	143.91 (2)	151.33 (6)
χ^2	1.038	2.581	3.812
R_P (%)	8.27	16.76	14.37
R_{WP} (%)	10.98	21.10	19.87
$\langle r_A \rangle$ (\AA)	1.109	1.142	1.175
τ	0.515	0.522	0.529

Note that $\langle r_A \rangle$ are calculated from ionic radii $r(\text{Nd}) = 1.109 \text{ \AA}$ and $r(\text{Bi}) = 1.24 \text{ \AA}$.

Figure 3 illustrates the 3D representation of the compound of $\text{Nd}_{1-x}\text{Bi}_x\text{MnO}_3$, which shows an octahedral MnO_6 , constructed using Visualisation for Electronic and Structural Analysis (VESTA) software. In this structure, the compounds Nd^{3+} , Mn^{3+} cations and O^{2-} anions occupy the corner, body center and face center positions, respectively. The A site in the ABO_3 - type perovskite structure occupied by

Nd/Bi cations was surrounded by 12 oxygen ions, while the octahedral MnO_6 formed by the position of Mn ions at the B site was surrounded by six oxygen ions.

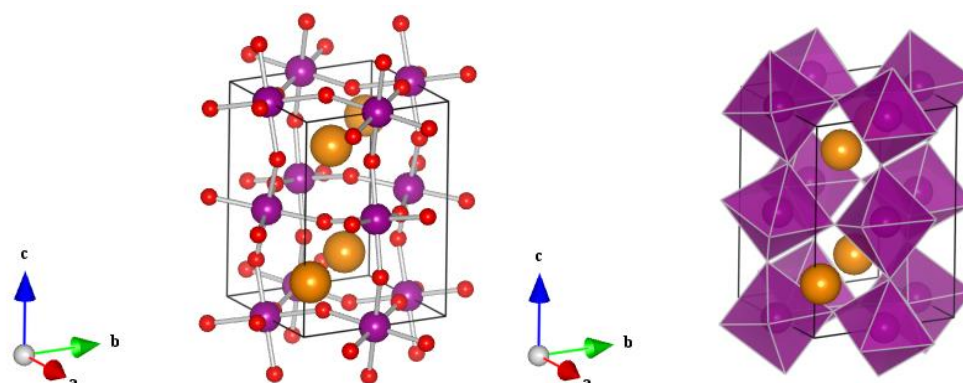


Figure 3. Crystallographic structure of NdMnO_3 . Purple, orange and red-colored balls represent the Mn, Nd and O, respectively.

3.2. FTIR Spectra

Figure 4 shows the spectra for the compound of NdMnO_3 doped with Bi in the frequency range from 450 cm^{-1} – 2000 cm^{-1} . From this figure, we can see that the most significant absorption bands are located at the range of 600 cm^{-1} – 550 cm^{-1} . The absorption bands at this range correspond to the Mn–O stretching vibration, linked to the internal movement of a length change of the bounds Mn–O–Mn, associated with the octahedron MnO_6 attributed to a vibration characteristics of the perovskite-type ABO_3 [3,19]. The absorption peak band at the range of 600 cm^{-1} – 550 cm^{-1} seem to shift towards lower wave number values for a structure having lower symmetry with decreasing Bi^{3+} ion content, according to the increase of e_g electrons in the anti-bonding orbital. Hence, the bond order would decrease with an increase in the number of e_g electrons. The lower frequency band can be related to a higher deformation mode of the MnO_6 octahedron [20,21]. The FTIR spectra confirm the formation of the NdBiMnO_3 sample.

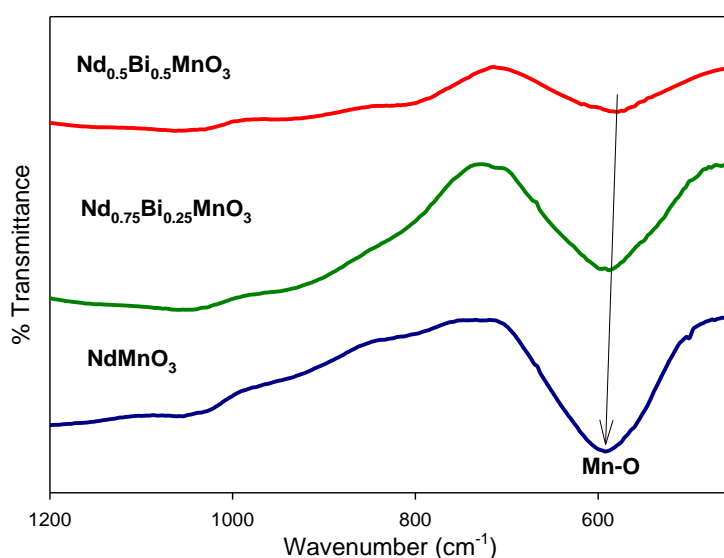


Figure 4. Fourier transform infrared spectroscopy (FTIR) spectra of $\text{Nd}_{1-x}\text{Bi}_x\text{MnO}_3$ ($x = 0, 0.25$ and 0.50).

3.3. Morphology

To understand the morphology of the samples, we performed FESEM with EDX and obtained the results, as shown in Figure 5. The images in Figure 5 reveal that the surface of the sample is

non-homogeneous and the grains are agglomerated. The particles are also observed as non-spherical in shape. According to the image, the grain size of all samples are in the range of $\sim 3.7 \mu\text{m}$ to $\sim 5.6 \mu\text{m}$, respectively. The grain sizes observed by FESEM are larger than those calculated by the Debye–Scherer formula. This can be explained by the fact that each particle observed by FESEM is formed by several crystallized grains. The results of EDX plot matches with a standard peak position of Nd, Bi, Mn and O from the previous study [19]. The EDX spectrum confirms the homogeneity of the samples.

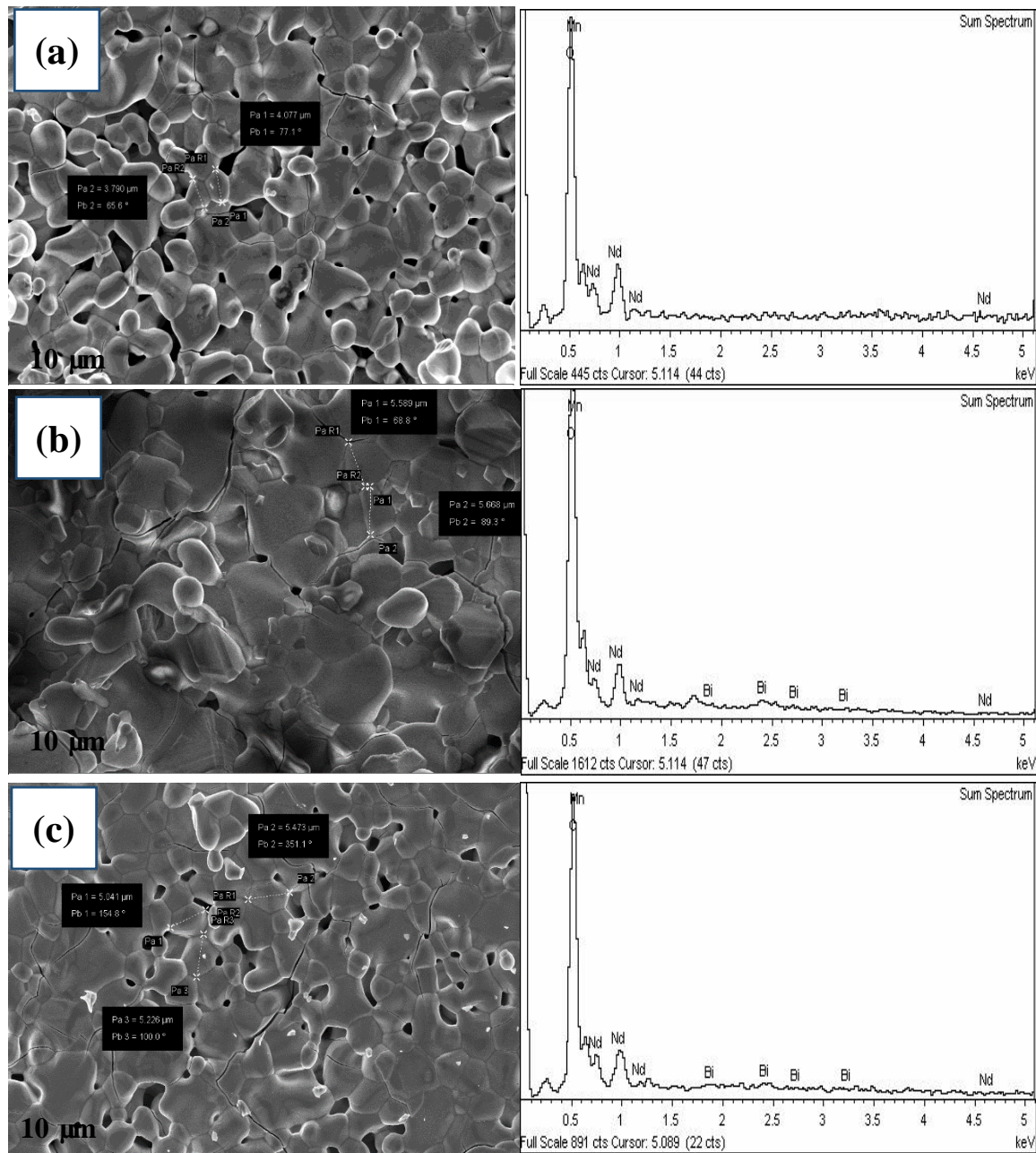


Figure 5. Field emission scanning electron microscopy (FESEM) micrograph and EDX spectra of $\text{Nd}_{1-x}\text{Bi}_x\text{MnO}_3$ (a) $x = 0$ (b) $x = 0.25$ and (c) $x = 0.5$.

3.4. AC Susceptibility Measurement

Figure 6 shows the temperature dependence of the AC susceptibility of the $\text{Nd}_{1-x}\text{Bi}_x\text{MnO}_3$ system on the real part χ' with the inset $d\chi'/dT$ versus the temperature range of 30–300 K. For $x = 0$ and $x = 0.25$, a definite and sharp peak was observed at 70 K and 72 K, respectively, associated to

the ordering temperature of Mn spins [22]. The observed cusp depicts the PM to AFM transition, which is consistent with the results from previous studies [5,8,23]. For $x = 0.50$, two sharp peaks were observed, which were at 42 K and 57 K, respectively. The existence of two peaks indicates the magnetic inhomogeneity that may be induced by Bi substitution [12]. The T_C was determined using the minimum, while T_N was determined using the maximum point of differentiation, as shown in the inset of the graph in Figure 6. In the figure, all the three compounds exhibit a strong AFM with a competing weak FM, where T_N and T_C decreased with Bi substitution. The decreasing value of T_C shows the weakening of the FM behavior due to the Bi substitution. Temperature dependence of inverse susceptibility, $1/\chi'$, for all samples is plotted in Figure 7. The experimental data were fitted by using Curie–Weiss (C–W) equation, $\chi = C/(T - \theta)$, where C is Curie constant and θ is Curie–Weiss temperature. The red line is the best fit for C–W law in the paramagnetic region. The inverse susceptibility curve follows the C–W law at the higher temperature and starts to deviate from the linear fitting of C–W law at the lower temperature above T_C , which shows the existence of Griffiths phase (GP) in the samples [24,25]. The deviation shows that the C–W law is inapplicable in the temperature range between T_C and Griffiths temperature, T_G ($T_C < T < T_G$). This anomaly indicates the possible existence of ferromagnetic cluster within the paramagnetic region in the system which would enhance the total magnetic susceptibility of the samples [24–27]. The temperature ranges of Griffiths phase normalized with T_C were evaluated using the equation $GP = (T_G - T_C)/T_C$ and were found to increase as the substitution of Bi increased. The increasing values were due to an increase of magnetic inhomogeneity near T_C . Therefore, the substitution of Bi in $Nd_{1-x}Bi_xMnO_3$ system could enhance the appearance of Griffiths phase [24]. The values of T_C , T_N , T_G and GP are summarized in Table 3.

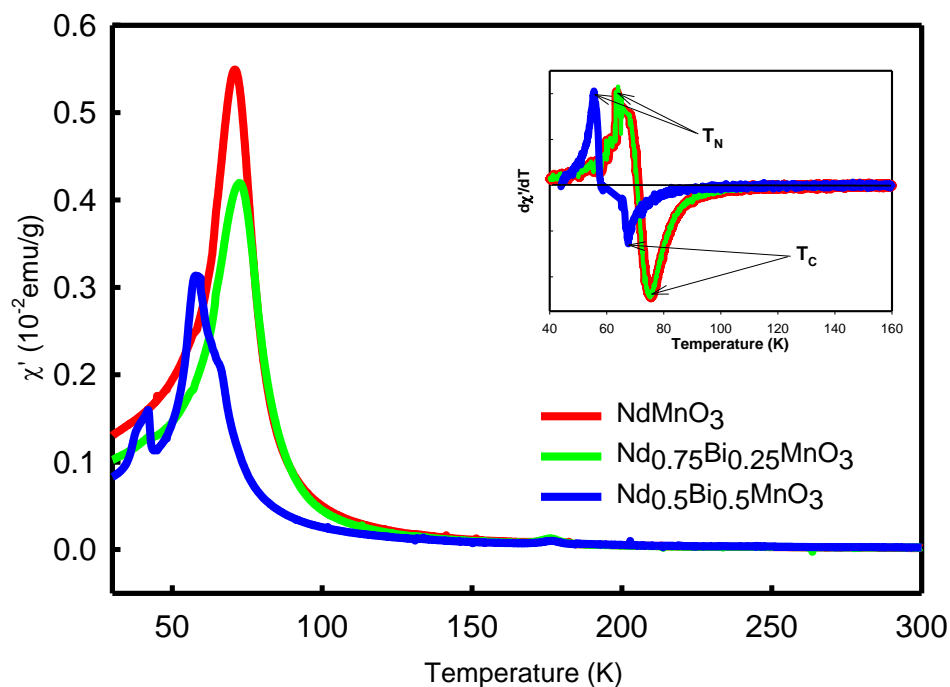


Figure 6. AC magnetic susceptibility against temperature curves for $Nd_{1-x}Bi_xMnO_3$.

Table 3. Parameters obtained from AC magnetic susceptibility studies of $Nd_{1-x}Bi_xMnO_3$ samples.

x	0	0.25	0.50
T_N (K)	64	64	55
T_C (K)	76	75	67
T_G (K)	181	198	182
GP (K)	138	164	171

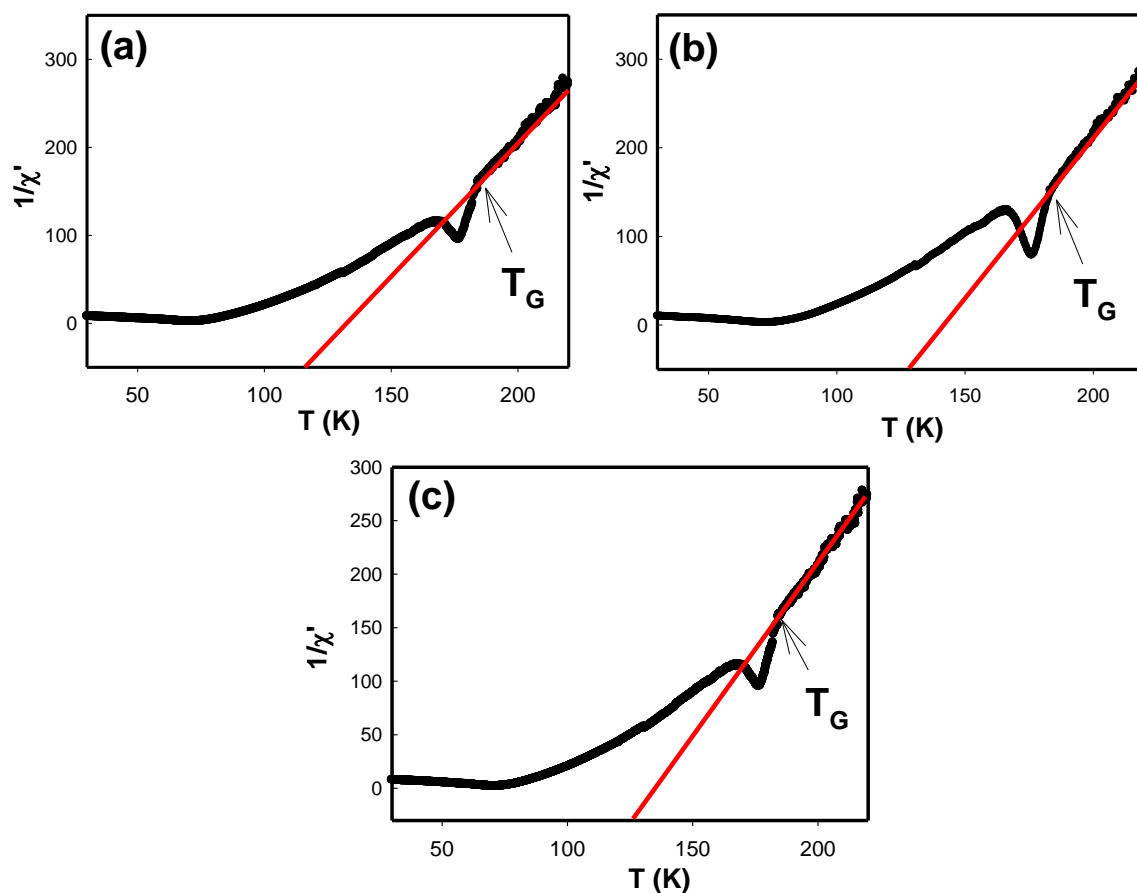


Figure 7. Temperature dependence of inverse susceptibility spectra of $\text{Nd}_{1-x}\text{Bi}_x\text{MnO}_3$ (a) $x = 0$, (b) $x = 0.25$ and (c) $x = 0.5$.

4. Conclusions

In summary, this study investigates the effect of Bi^{3+} substitution on structural, optical, morphological and magnetic properties of $\text{Nd}_{1-x}\text{Bi}_x\text{MnO}_3$ samples. The XRD analysis and Rietveld refinement show the pattern corresponding to the perovskite-type NdMnO_3 , which crystallizes in the orthorhombic system with main peak at (121) hkl plane with the Pbnm space group. The structural parameter and cell volume of the samples increase as the Bi^{3+} content increases. In addition, the average ionic radii of A site, $\langle r_A \rangle$, increased, hence τ also increased. The FTIR spectra show that active vibrational bands present at 600 cm^{-1} – 550 cm^{-1} , which correspond to the metal oxide Mn–O stretching vibration of perovskite NdMnO_3 . FESEM images show that the sample is non-spherical and somewhat agglomerated. The samples show a strong AFM behavior at low temperature with decreasing T_C due to the Bi substitution. Deviation of temperature dependence of inverse susceptibility curves shows the existence of Griffiths phase in these materials.

Author Contributions: Z.M. conceived and designed the experiment; I.S.I. performed the experiments supervised by Z.M. The manuscript was written by N.A.A. and Z.M. with contributions from N.B.M. and A.H. All authors have read and agreed to the published version of the manuscript.

Funding: This research was financially supported by the Ministry of Education Malaysia (MOE) and Universiti Teknologi MARA, grant number 600-IRMI/FRGS-RACER 5/3 (042/2019).

Acknowledgments: The authors would like to thanks the Faculty of Applied Sciences, Universiti Teknologi MARA for FESEM and FTIR characterization, and Center for Superconducting & Magnetic Novel Oxides of Universiti Teknologi MARA for ACS characterization.

Conflicts of Interest: The authors declare no conflict of interest.

References

1. Massa, N.E.; Campo, L.; Meneses, D.D.S.; Martínez-lope, M.J.; Alonso, J.A. High temperature far infrared dynamics of orthorhombic NdMnO₃; emissivity and reflectivity. *J. Phys. Condens. Matter.* **2013**, *25*, 235603. [[CrossRef](#)] [[PubMed](#)]
2. Renwen, Q.; Zhe, L.; Jun, F. Influence of Bi³⁺ doping on electronic transport properties of La_{0.5x}Bi_xCa_{0.5}MnO₃ manganites. *Phys. B Phys. Condens. Matter.* **2011**, *406*, 1312–1316.
3. Hernández, E.; Sagredo, V.; Delgado, G.E. Synthesis and magnetic characterization of LaMnO₃ nanoparticles. *Rev. Mex. Fis.* **2015**, *61*, 166–169.
4. Ahmadvand, H.; Salamati, H.; Kameli, P. The effect of grain boundaries on the domain wall dynamics in Pr_{1-x}Ag_xMnO₃ manganites. *J. Appl. Phys.* **2010**, *107*, 083913. [[CrossRef](#)]
5. Nandy, A.; Roychowdhury, A.; Das, D.; Pradhan, S.K. Structural and magnetic characterizations of undoped and K-doped NdMnO₃ single crystals synthesized by sol-gel route: A comparative study. *Powder Technol.* **2014**, *254*, 538–547. [[CrossRef](#)]
6. Chatterji, T.; Ouladdiaf, B.; Bhattacharya, D. Neutron diffraction investigation of the magnetic structure and magnetoelastic effects in NdMnO₃. *J. Phys. Condens. Matter.* **2009**, *21*, 1–6. [[CrossRef](#)]
7. Liu, K.; Wu, X.W.; Ahn, K.H.; Sulchek, T.; Chien, C.L.; Xiao, J.Q. Charge ordering and magnetoresistance in Nd_{1-x}Ca_xMnO₃ due to reduced double exchange. *Phys. Rev. B* **1996**, *54*, 3007. [[CrossRef](#)]
8. Wu, S.Y.; Hwang, S.R.; Li, W.; Lee, K.C.; Lynn, J.W.; Liu, R.S. Jahn-Teller distortion, charge ordering, and magnetic transitions in Ca-Doped NdMnO₃. *J. Phys.* **2000**, *38*, 354–359.
9. Arifin, M.; Ibrahim, N.; Mohamed, Z.; Yahya, A.K.; Khan, N.A.; Khan, M.N. Revival of metal-insulator and ferromagnetic-paramagnetic transitions by Ni substitution at Mn site in charge-ordered monovalent doped Nd_{0.75}Na_{0.25}MnO₃ manganites. *J. Supercond. Nov. Magn.* **2018**, *31*, 2851–2868. [[CrossRef](#)]
10. Tang, T.; Tien, C.; Hou, B.Y. Electrical transport and magnetic properties of Nd_{1-x}Na_xMnO₃ manganites. *J. Alloys Compd.* **2008**, *461*, 42–47. [[CrossRef](#)]
11. Chiba, H.; Atou, T.; Syono, Y. Magnetic and Electrical Properties of Bi_{1-x}Sr_xMnO₃: Hole-Doping Effect on Ferromagnetic Perovskite BiMnO₃. *J. Solid State Chem.* **1997**, *132*, 139–143. [[CrossRef](#)]
12. Ghani, M.A.; Mohamed, Z.; Yahya, A.K. Effects of Bi substitution on magnetic and transport properties of La_{0.7-x}Bi_xAg_{0.3}MnO₃ ceramics. *J. Supercond. Nov. Magn.* **2012**, *25*, 2395–2402. [[CrossRef](#)]
13. Zhao, Y.D.; Park, J.; Jung, R.J.; Noh, H.J.; Oh, S.J. Structure, magnetic and transport properties of La_{1-x}Bi_xMnO₃. *J. Magn. Magn. Matter.* **2004**, *280*, 404–411. [[CrossRef](#)]
14. Sugawara, F.; Iiida, S. Magnetic properties and crystal distortions of BiMnO₃ and BiCrO₃. *J. Phys. Soc. Jpn.* **1968**, *25*, 1553–1558. [[CrossRef](#)]
15. Lalitha, G.; Reddy, P.V. Low temperature resistivity anomalies in bismuth doped manganites. *J. Alloys Compd.* **2010**, *494*, 476–482. [[CrossRef](#)]
16. Alonso, J.A.; Martínez-Lope, M.J.; Casais, M.T.; Fernández-Díaz, M.T. Evolution of the Jahn-Teller distortion of MnO₆ octahedra in RMnO₃ perovskites (R = Pr, Nd, Dy, Tb, Ho, Er, Y): A neutron diffraction study. *Inorg. Chem.* **2000**, *39*, 917–923. [[CrossRef](#)]
17. Srivastava, S.R.S.K. Magnetic properties of Nd_{1-x}Ag_xMnO₃ compounds. *J. Phys. Condens. Matter.* **2008**, *20*, 505212. [[CrossRef](#)]
18. Sangale, M.D.; Gaikwad, D.N.; Sonawane, D.V.; Suryavanshi, D.M. Synthesis and characteristic properties of perovskite-type NdMnO₃ nanocrystal materials via a co-precipitation method. *J. Chem. Phys. Sci.* **2018**, *7*, 291–296.
19. Somvanshi, A.; Husain, S. Study of structural, dielectric and optical properties of NdMnO₃. *AIP Conf. Proc.* **2018**, *1953*, 1–5.
20. Turkey, A.O.; Rashad, M.M.; Hassan, A.M.; Elnaggar, E.M.; Bechelany, M. Optical, electrical and magnetic properties of lanthanum strontium manganite La_{1-x}Sr_xMnO₃ synthesized through the citrate combustion method. *Phys. Chem. Chem. Phys.* **2017**, *19*, 6878–6886. [[CrossRef](#)]
21. Mohamed, Z.; Shahron, I.S.; Ibrahim, N.; Maulud, M.F. Influence of ruthenium doping on the crystal structure and magnetic properties of Pr_{0.67}Ba_{0.33}Mn_{1-x}Ru_xO₃ Manganites. *Crystal* **2020**, *10*, 295. [[CrossRef](#)]
22. Wu, S.Y.; Kuo, C.M.; Wang, H.Y.; Li, W.-H.; Lee, K.C. Magnetic structure and spin reorientation of the Mn ions in NdMnO₃. *J. Appl. Phys.* **2000**, *87*, 5822–5824. [[CrossRef](#)]

23. Asmira, N.; Ibrahim, N.; Mohamed, Z.; Yahya, A.K. Effect of Cr^{3+} substitution at Mn-site on electrical and magnetic properties of charge ordered $\text{Bi}_{0.3}\text{Pr}_{0.3}\text{Ca}_{0.4}\text{MnO}_3$ manganites. *Phys. B Condens. Matter*. **2018**, *544*, 34–46. [[CrossRef](#)]
24. Manjunatha, S.O.; Rao, A.; Poornesh, P.; Lin, W.J.; Kuo, Y.K. Magnetic inhomogeneity and Griffiths phase in Bi substituted $\text{La}_{0.65-x}\text{Bi}_x\text{Ca}_{0.35}\text{MnO}_3$ manganites. *Phys. B Condens. Matter*. **2016**, *498*, 82–91. [[CrossRef](#)]
25. Zheng, X.; Gao, T.; Jing, W.; Wang, X.Y.; Liu, Y.S.; Chen, B.; Dong, H.L.; Chen, Z.Q.; Cao, S.X.; Cai, C.B.; et al. Evolution of Griffiths phase and spin reorientation in perovskite manganites. *J. Magn. Magn. Mater.* **2019**, *491*, 165611. [[CrossRef](#)]
26. Pękała, M.; Szydłowska, J.; Pękała, K.; Drozd, V. Griffiths like phase in nanocrystalline manganite $\text{La}_{0.50}\text{Ca}_{0.50}\text{MnO}_3$ studied by magnetic susceptibility and electron spin resonance. *J. Alloys Compd.* **2016**, *685*, 237–241. [[CrossRef](#)]
27. Elyana, E.; Mohamed, Z.; Kamil, S.A.; Supardan, S.N.; Chen, S.K.; Yahya, A.K. Revival of ferromagnetic behavior in charge-ordered $\text{Pr}_{0.75}\text{Na}_{0.25}\text{MnO}_3$ manganite by ruthenium doping at Mn site and its MR effect. *J. Solid State Chem.* **2018**, *258*, 191–200. [[CrossRef](#)]



© 2020 by the authors. Licensee MDPI, Basel, Switzerland. This article is an open access article distributed under the terms and conditions of the Creative Commons Attribution (CC BY) license (<http://creativecommons.org/licenses/by/4.0/>).